nature geoscience

ARTICLES

https://doi.org/10.1038/s41561-017-0054-8

Pathways to 1.5 °C and 2 °C warming based on observational and geological constraints

Philip Goodwin[1*], Anna Katavouta[2], Vassil M. Roussenov[2], Gavin L. Foster[1], Eelco J. Rohling[1,3] and Richard G. Williams[2]

To restrict global warming to below the agreed targets requires limiting carbon emissions, the principal driver of anthropogenic warming. However, there is significant uncertainty in projecting the amount of carbon that can be emitted, in part due to the limited number of Earth system model simulations and their discrepancies with present-day observations. Here we demonstrate a novel approach to reduce the uncertainty of climate projections; using theory and geological evidence we generate a very large ensemble (3×10^4) of projections that closely match records for nine key climate metrics, which include warming and ocean heat content. Our analysis narrows the uncertainty in surface-warming projections and reduces the range in equilibrium climate sensitivity. We find that a warming target of 1.5 °C above the pre-industrial level requires the total emitted carbon from the start of year 2017 to be less than 195–205 PgC (in over 66% of the simulations), whereas a warming target of 2 °C is only likely if the emitted carbon remains less than 395–455 PgC. At the current emission rates, these warming targets are reached in 17–18 years and 35–41 years, respectively, so that there is a limited window to develop a more carbon-efficient future.

The Paris Agreement[1] aspires to restrict the rise in global mean surface temperature since the pre-industrial period to 2 °C or less for this century by reducing global carbon emissions, the principal driver of anthropogenic warming[2]. However, there are large uncertainties in how much carbon may be emitted before meeting a warming target[3]. For example, a subset of 13 Earth system models[4,5] (from the Climate Model Intercomparison Project phase 5 (CMIP5)) suggests that a 2 °C warming may be met by cumulative carbon emissions that range from 84 to 581 PgC from year 2017 following the Representative Concentration Pathway (RCP)[6] 8.5 (Fig. 1a and Supplementary Table 1). A large ensemble of simple climate model simulations[7] obtained an even wider uncertainty range for the maximum permitted cumulative carbon emission to avoid a 1.5 °C warming, which ranged from at least 250 to 540 PgC from year 2015 in 33% of their simulations (and extended even further from less than 200 to more than 850 PgC in 66% of their simulations). Clearly, the large uncertainties in a permitted future carbon budget to meet specific warming targets need to be reduced.

In our view, a significant part of the large uncertainties in how much carbon may be emitted is due to discrepancies between model simulations and historical data. CMIP5 models are powerful tools to explore warming projections, solve the climate response to radiative forcing and provide emergent properties, such as the equilibrium climate sensitivity. However, there are mismatches between the CMIP5 simulations and historical reconstructions; for example, model projections of surface temperature differ from historical records[8–12] (Figs. 1b and 2a (grey band)) with an average model–data mismatch of 0.2 °C (for the time-averaged temperature anomaly from the late nineteenth century time average and the period 1986 to 2005), and several models have too high a global ocean heat content from year 1980 onward compared with observational reconstructions[13–18] (Fig. 1c). Such discrepancies with observation-based reconstructions introduce uncertainty into future warming projections, which could be biased towards either too much or too little warming.

Generating observationally constrained warming projections. Here we present a complementary approach to make twenty-first century projections of surface-warming projections, which is designed to minimize the model–data mismatch for the historical record. We exploit our theory for how warming connects to carbon emissions[19,20] to drive an efficient Earth system model (the Warming, Acidification and Sea-level Projector[21,22] (Methods)). Using geological evidence[23] for the equilibrium climate sensitivity, we produced an ensemble of climate simulations that spans the uncertainty in observational reconstructions of warming[8–12], ocean heat uptake[13–18] and carbon fluxes[2,24]. Our approach is similar to the 'history matching' approach applied to statistical emulators of complex Earth system models[25,26], except that here we use an efficient mechanistic Earth system model in place of a statistical emulator.

Our theory[19,20] demonstrates how the global mean surface temperature anomaly relative to the pre-industrial temperature at time t, $\Delta T(t)$, is related to cumulative carbon emissions, $I_{\mathrm{em}}(t)$ (PgC), and the weighted sum[27–29] of radiative forcing from all forcing agents since pre-industrial times, $\Delta R_{\mathrm{total}}^{\mathrm{weighted}}(t)$ (W m^{-2}), modified by the planetary heat uptake and the changes in ocean and terrestrial carbon inventories:

$$\Delta T(t)=\frac{aS}{I_B}\left(1-\frac{\varepsilon_N N(t)}{\Delta R_{\mathrm{total}}^{\mathrm{weighted}}(t)}\right)\left(\frac{\Delta R_{\mathrm{total}}^{\mathrm{weighted}}(t)}{\Delta R_{\mathrm{CO_2}}(t)}\right)\\(I_{\mathrm{em}}(t)+I_{\mathrm{Usat}}(t)-\Delta I_{\mathrm{ter}}(t)),\qquad(1)$$

where $a=5.35\pm0.27$ W m^{-2} is the CO_2-radiative forcing coefficient[2], S (K (W m^{-2})$^{-1}$) is an empirically determined[30] climate sensitivity, $N(t)$ (W m^{-2}) is the planetary heat uptake, which effectively represents ocean heat uptake, $\Delta R_{\mathrm{CO_2}}(t)$ (W m^{-2}) is the radiative forcing from CO_2, ε_{N} is a non-dimensional weighting (referred to as the efficacy) for ocean heat uptake[30], I_{Usat} (PgC) is

[1]Ocean and Earth Science, National Oceanography Centre Southampton, University of Southampton, Southampton, UK. [2]Department of Earth, Ocean & Ecological Sciences, School of Environmental Sciences, University of Liverpool, Liverpool, UK. [3]Research School of Earth Sciences, Australian National University, Canberra, ACT, Australia. *e-mail: p.a.goodwin@soton.ac.uk

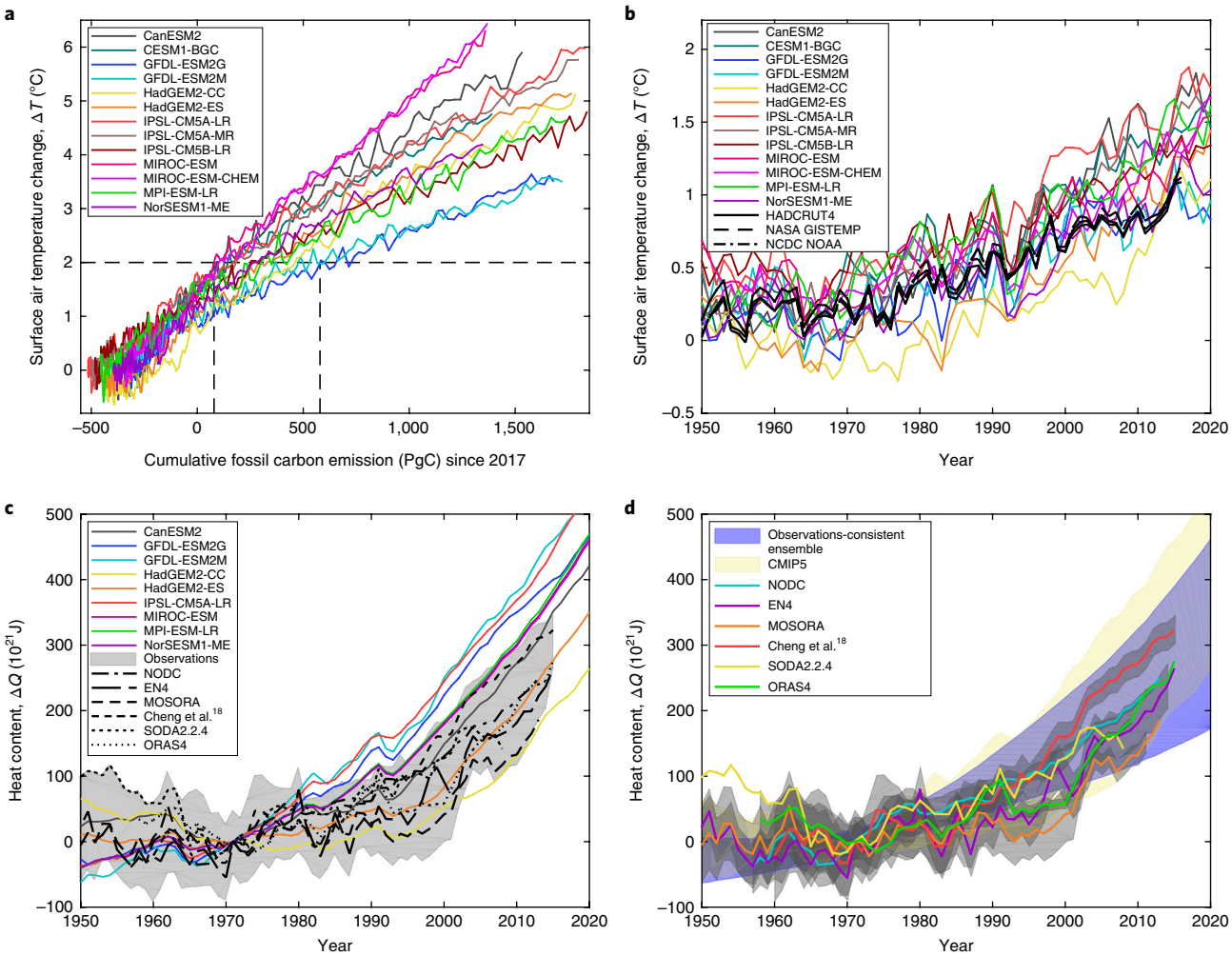

Fig. 1 | Surface warming projections and ocean heat content anomalies. a, Global surface air temperature anomaly from 13 Earth system models relative to the late-nineteenth-century time average (Methods) from years 1861 to year 2100 following RCP8.5 (lines) versus cumulative fossil-fuel carbon emissions since year 2017. The dashed lines indicate when the projected warming exceeds 2 °C in cumulative fossil-fuel emission. **b**, Global surface air temperature anomaly relative to the late-nineteenth-century time average (Methods) versus time from three different data-based reconstructions and 13 Earth system models from year 1950 to year 2016 (observations) and to 2020 (models) following RCP8.5 (lines). **c**, Historical reanalyses for global ocean heat content, ΔQ (10^{21} J) over the full depth relative to 1971 from available observational analyses and reanalysis products, together with nine different CMIP5 model variants (lines). **d**, ΔQ (10^{21} J) over the full depth relative to 1971 for nine different CMIP5 Earth system models (yellow shading) and the observation-consistent ensemble of our conceptual Earth system model simulations (blue shading) with projections up to year 2020. ΔQ for NODC and Cheng et al.[18] are for 0–2,000 m depth, whereas the others are full-depth. The grey shaded areas show the uncertainty for the heat content anomalies.

the global ocean undersaturation of dissolved inorganic carbon[19] with respect to instantaneous atmospheric CO_2, ΔI_{ter} (in PgC) is the cumulative change in residual terrestrial carbon storage since the pre-industrial period, and I_B (PgC) is the pre-industrial buffered carbon inventory of the global atmosphere and ocean system[19], of around 3,500 PgC. The climate sensitivity, S, is related to the equilibrium climate sensitivity, ΔT_{2xCO2}, which defines the surface air temperature change for a sustained doubling of atmospheric CO_2, by $S = \Delta T_{2xCO2}/(a \ln 2)$. In equation (1), the efficacy of ocean heat uptake, ε_N, accounts for how the heat uptake $N(t)$ may have a different impact on $\Delta T(t)$ than an equivalent radiative forcing from CO_2, $\Delta R_{CO2}(t)$ (ref. [30]), whereas radiative forcing from aerosols and non-well-mixed greenhouses gases may be weighted[27–29] (with an efficacy, ε_i, that differs from 1), such that $\Delta R_{total}^{weighted}(t) = \Delta R_{CO_2}(t) + \Sigma \varepsilon_i \Delta R_i(t)$, where i sums over all other forcing agents, $\varepsilon_i = 1$ for well-mixed greenhouse gases and ε_i is referred to as ε_{aero} for aerosols.

Our efficient Earth system model[21,22] exploits our surface warming relationship (equation (1)) to make climate simulations from the pre-industrial period and projections for the twenty-first century. The model assumes that the empirical parameters a, S, and I_B, and the non-dimensional weightings ε_N and ε_i, are constant with time, and then applies these parameters within an eight-box representation of the atmosphere–ocean–terrestrial system[21] (Methods). The model solves, with time, for the global surface temperature anomaly, $\Delta T(t)$, planetary heat uptake, $N(t)$, carbon emissions, $I_{em}(t)$, ocean carbon undersaturation, $I_{Usat}(t)$ and residual terrestrial carbon storage, $\Delta I_{ter}(t)$, for the prescribed CO_2 and radiative forcing pathways[21,22] (equation (1) and Methods).

First, we used our efficient Earth system model to generate 10^8 simulations integrated from year 1765 to year 2016, where each simulation has a unique set of 18 model parameter values that are varied independently between the simulations (Methods and Supplementary Table 2). The prior choices of the climate sensitivity,

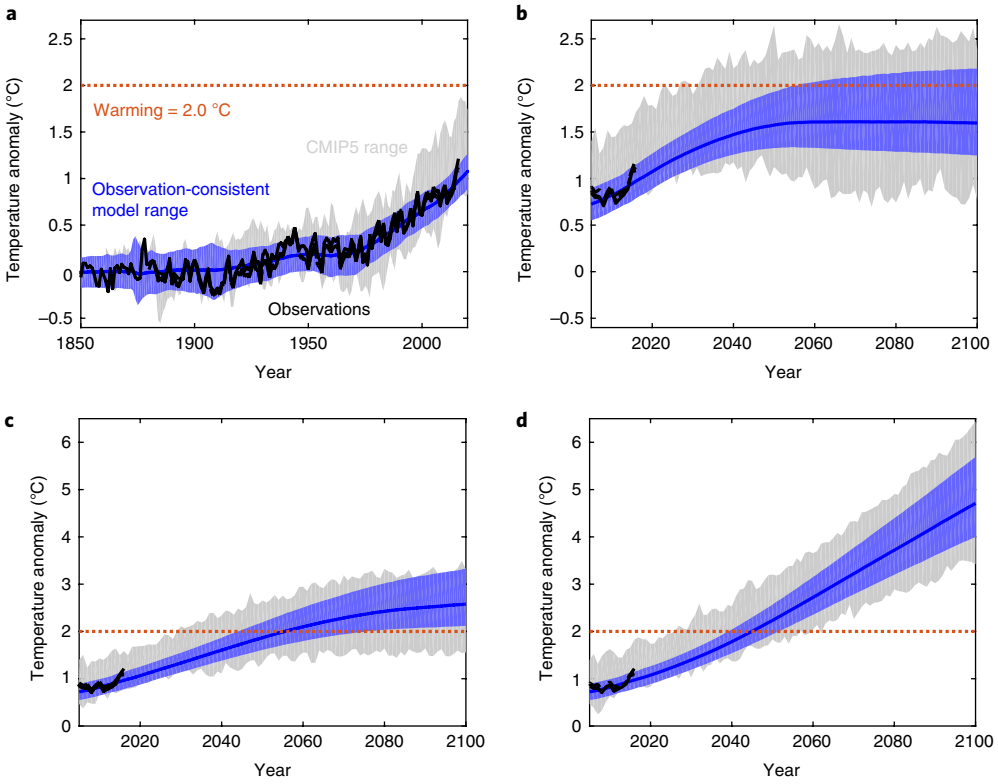

Fig. 2 | Global mean surface temperature anomaly over time from observations and model simulations. The temperature anomaly relative to the late nineteenth century time average for three observational records (black lines, as in Fig. 1b), the range of selected CMIP5 Earth system models (grey shaded areas) and the observation-consistent ensemble from our efficient Earth system model (the blue shaded area is the 95% range and the blue line is the median). **a**, Historical temperature anomaly (years 1861–2020). **b**–**d**, Years 2005–2100 for RCP2.6 (**b**), RCP4.5 (**c**) and RCP8.5 (**d**). The model simulations in **a** employ the high-end RCP8.5 scenario to extend to the year 2020.

S, and resulting equilibrium climate sensitivity, ΔT_{2xCO2}, were taken from a frequency-density distribution of a geological reconstruction for the Cenozoic[23] (about the past 65 Ma), with *S* ranging from 0.48 to 1.96 K $(W m^{-2})^{-1}$ and ΔT_{2xCO2} from 1.8 to 7.3 °C at 95% bounds (Fig. 3, black solid lines). This initial set of 10^8 simulations was then tested for consistency against observations (Supplementary Table 3), using nine observational constraints of historic warming[8–12], ocean heat content[13–18] (Supplementary Table 4) and carbon-flux reconstructions[2,24]. Only 3×10^4 simulations (0.03%) passed the full consistency test, and they formed our 'realistic ensemble' of simulations that are consistent with historical records (Supplementary Table 3) and within uncertainty bounds for ocean heat uptake (Fig. 1c,d), surface warming (Figs. 1 and 2a (black line)), and ocean and terrestrial carbon uptake (Supplementary Fig. 1).

Second, the 3×10^4 observation-consistent configurations of our efficient Earth system model were integrated forward from the start of year 2017 to year 2100 for atmospheric CO_2, following standard RCP scenarios and including forcing of non-CO_2 greenhouse gases and aerosols[6] (Methods and Supplementary Table 3), and retained the historic uncertainty in radiative forcing from different sources (Supplementary Fig. 2).

Observationally consistent pathways towards warming targets. The observation-consistent simulations reach a surface temperature anomaly of 2 °C above the late nineteenth century average between years 2040 and 2052 for RCP8.5 (Fig. 2d, 95% confidence bands). Regarding other pathways, a 2 °C warming is only slightly delayed to between years 2045 and 2076 for RCP4.5 (Fig. 2c), whereas most simulations (93%) remain under a 2 °C warming by year 2100 for RCP2.6 (Fig. 2b). In comparison, the International Panel on Climate Change (IPCC) AR5 Earth system model ensemble suggests that a 2 °C warming occurs within a much wider window between years 2026 and 2063 for RCP8.5; in addition, 22% of the AR5 models suggest that RCP4.5 might be sufficient to remain below a 2 °C warming target through the twenty-first century (compared with the less than 1% of simulations for our observation-consistent ensemble).

Next, we assessed the statistical likelihood of restricting surface warming to a maximum of 1.5 or 2.0 °C, in terms of the additional cumulative carbon emitted from the start of year 2017 (Fig. 4). For a given future cumulative carbon emission, our ensemble projections indicate that warming is 'likely' to be below a given target if at least 66% of simulations agree (adopting AR5 terminology[2]). A surface warming of 1.5 °C remains likely until cumulative carbon emissions reach between 195 and 205 PgC from the start of year 2017 (Fig. 4a, b and Table 1). A surface warming of 2.0 °C or less remains likely until the cumulative carbon emission reaches 395 to 455 PgC from the start of year 2017 (Fig. 4a,c and Table 1). By the time cumulative carbon emissions reach 540 PgC from year 2017, more than 75% of the projections have a warming of 2.0 °C or more for both RCP8.5 and RCP4.5. Assuming our current carbon emission rate[24], the 1.5 °C warming target is likely to occur in 17–18 years and the 2 °C warming target is likely to be reached in 35–41 years. In comparison, by only allowing observation-consistent ensemble simulations, our range for the maximum permitted carbon emission for a 1.5 °C target is more restrictive than a recent large ensemble of climate model simulations[7], which instead suggested a higher possible permitted cumulative carbon emission of at least 250 to 540 PgC from year 2015.

Reducing uncertainty in climate sensitivity and future warming. Our observationally consistent projections of a future surface

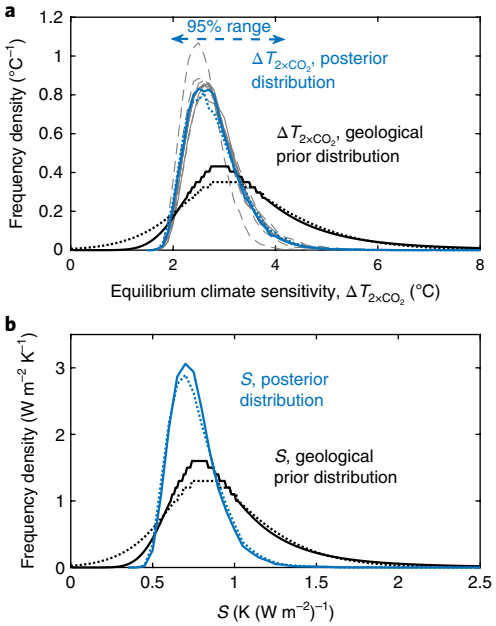

Fig. 3 | Model ensemble parameter distributions. a, Equilibrium climate sensitivity. **b**, Climate sensitivity. Input distributions in the initial 10^8 efficient Earth system model simulations (black) and the final distribution in the 10^4 observation-consistent simulations for RCP8.5 (blue). The climate sensitivity parameter, *S*, where the input distribution is taken from geological evidence (black solid line) and for the final geologically and observationally constrained ensemble (blue solid line). The different distributions are included for the alternative geological reconstruction input distribution (black dotted line) and resulting alternative observationally constrained ensemble (blue dotted line) and the observation-constrained ensembles for the other RCP scenarios (grey solid lines) and the perturbation experiments for RCP8.5 (grey dashed lines) (Supplementary Table 5).

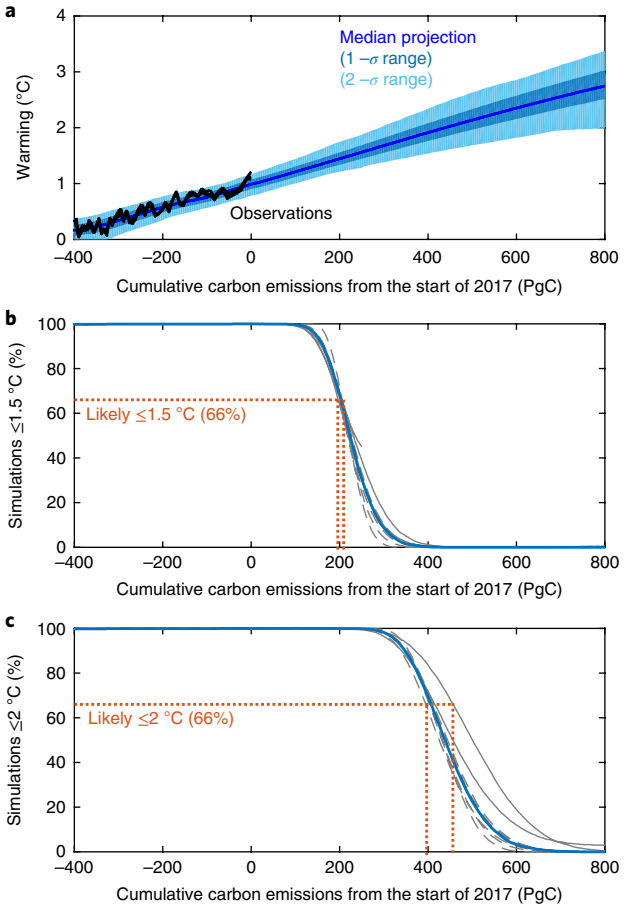

Fig. 4 | Cumulative carbon emissions and warming projections from our observationally consistent ensemble. a, Global mean surface temperature anomaly relative to the year 1850 to 1900 average against cumulative carbon emitted since the start of year 2017. Shown are the observation-consistent ensemble (blue line and dark blue shaded area are the median and 66% range for the RCP8.5 standard experiment, respectively; the light blue shading is the 95% range across all RCP scenarios for the standard experimental configuration (Methods)) and the observations (black lines as in Fig. 1b). For the observational reconstructions (black lines), cumulative carbon emissions prior to year 2017 are calculated from the Global Carbon Project reconstructions[24] and warming is from the three reconstructions as in Fig. 1b. **b**,**c**, The percentage of observationally constrained simulations that remain with warming of 1.5 °C or under (**b**) and 2 °C or under (**c**) relative to the year 1850 to year 1900 average against additional carbon emitted since the start of year 2017. The solid blue line is the RCP8.5 standard experiment, grey solid lines are the standard experiments with alternative RCP scenarios and grey dashed lines are for alternative input distribution experiments (Methods).

temperature anomaly make different underlying assumptions to those made for complex Earth system models[2,5], and so the two approaches are complementary.

The CMIP5-based projections[2,5], based on complex Earth system models, solve for the climate response and their emergent properties, which include climate sensitivity[31–35] and the non-dimensional weightings of radiative forcings[27–29] and heat imbalances[30,36], ε_i and ε_N (equation (1)). Intermodel differences[37] in their projections arise from differences in their emergent equilibrium climate sensitivity, and in how each model takes up heat and carbon, and non-CO_2 radiative forcing. However, there are differences between the CMIP5-based projections over the historical record and the observations (Fig. 1b,c).

In contrast, our projections are designed to lie within the uncertainty bounds of the historical observations, including for warming and heat uptake. However, our projections require prior input distributions for model parameters, including climate sensitivity and the non-dimensional efficacy weightings, ε_i and ε_N, which are then held constant in time.

We then performed a set of perturbation experiments to test the robustness of our results with respect to the prior distributions of model parameters in the initial 10^8 simulations (Methods and Supplementary Table 5). These perturbation experiments use six alternative input distributions as the model parameters, including an alternative geological distribution[23] for climate sensitivity, *S* (Fig. 3, black dotted lines), and alternative distributions for the efficacy of heat uptake, ε_N, the efficacy of aerosol radiative forcing, ε_{aero}, and the uncertainty in the radiative forcing from aerosols. These perturbation experiments support our inferences for projected warming from the default experiment (Fig. 4, compare the grey and blue lines (Supplementary Table 6)). Across all the perturbation experiments for RCP8.5, the maximum cumulative emission at which 66% of the simulations remain under a warming target of 1.5 °C only varied between 195 and 205 PgC and under a warming target of 2 °C only varied between 395 and 405 PgC from the start of year 2017 (Table 1).

Within our ensemble of observation-consistent simulations, both the variation in warming projections and posterior equilibrium climate sensitivity are correlated with the simulated values of multiple historical constraints (Methods, Supplementary Fig. 4 and Supplementary Table 8). Warming projections are the most correlated to historic simulated temperature change ($R^2 = 0.2$), but are

Table 1 | Cumulative emissions from year 2017 when the 1.5 °C and 2 °C warming targets are exceeded for the standard modelling experiment and perturbation experiments, including different choices of climate sensitivity, *S*, ε_N, ε_{aero} and aerosol radiative forcing (full details in Supplementary Tables 5 and 6)

Experiment	Maximum emissions for warming ≤1.5 °C in 66% of simulations	Maximum emissions for warming ≤1.5 °C in 50% of simulations (5–95%)	Maximum emissions for warming ≤2 °C in 66% of simulations	Maximum emissions for warming ≤2 °C in 50% of simulations (5–95%)
(1) Standard experiment	200 PgC	220 PgC (145 to 315)	405 PgC	435 PgC (320 to 580)
(2) Perturbation experiments for RCP8.5	195 to 205 PgC	215 to 225 PgC (135 to 325)	395 to 410 PgC	425 to 440 PgC (315 to 590)

Includes different choices of climate sensitivity, *S*, ε_N, ε_{aero} and aerosol radiative forcing (full details are given in Supplementary Tables 5 and 6). All non-standard experiments follow RCP8.5.

also correlated to simulated historic ocean heat uptake ($R^2 = 0.13$), whereas the equilibrium climate sensitivity is most correlated to ocean heat uptake ($R^2 = 0.3$) and then historic temperature change ($R^2 = 0.08$). Thus, for the model projections to have any skill, reconstructions of both historic surface temperature and ocean heat uptake are needed (Fig. 1b,c).

Climate sensitivity is a key model parameter in determining the projected warming within our ensemble (Methods and Supplementary Table 9). An improved posterior estimate of the climate sensitivity is obtained from our two-stage process of assuming a prior estimate from geological reconstructions and then updating by the observational-consistent simulations (Fig. 3). This posterior estimate of equilibrium climate sensitivity lies between 2.0 and 4.3 °C based on 95% of the observation-consistent ensemble of simulations (Fig. 3, blue and grey lines (Supplementary Table 7)). This posterior estimate is narrower than either of the prior distributions from geological evidence[23] (Fig. 3, black solid and dotted lines), and does not support the lowest values (from 1.5 to 2.0 °C) of the AR5 likely range[2] for an equilibrium climate sensitivity of 1.5 to 4.5 °C. This narrowing of the geological estimate[23] for climate sensitivity (Fig. 3) is interpreted as the historical constraints revealing the part of the climate sensitivity range for the entire Cenozoic[23] that is applicable for the present day.

Implications for the Paris Agreement. The Paris Agreement[1] aims to keep the global surface temperature anomaly within 2.0 °C of the pre-industrial one, and preferably close to 1.5 °C. Our analysis, using an observation-consistent ensemble of projections from an efficient Earth system model, is consistent with the observed trend between additional warming and cumulative emissions continuing into the future (Fig. 4a), and with previous studies that identified a near-linear link between warming and cumulative emissions[19,38–40] (Fig. 4a). Our projections suggest that a likely chance of meeting the 1.5 °C warming target requires that cumulative carbon emissions remain below 195 to 205 PgC from the start of 2017, whereas a 2 °C warming target requires that cumulative carbon emissions remain below 395 to 455 PgC. The 1.5 and 2 °C warming targets are reached in 17–18 years and in 35–41 years, respectively, if the carbon emission rate is assumed to remain at its present-day value. Hence, immediate action is required to develop a carbon-neutral or carbon-negative future[41,42] or, alternatively, prepare adaptation strategies for the effects of a warmer climate.

Methods

Methods, including statements of data availability and any associated accession codes and references, are available at https://doi.org/10.1038/s41561-017-0054-8.

Received: 7 July 2017; Accepted: 14 December 2017;
Published online: 22 January 2018

References

1. *Adoption of the Paris Agreement* FCCC/CP/2015/L.9/Rev.1 (UNFCCC, 2015).
2. IPCC *Climate Change 2013: The Physical Science Basis* (eds Stocker, T. F. et al.) (Cambridge Univ. Press, Cambridge, 2013).
3. Meinshausen, M. et al. Greenhouse-gas emission targets for limiting global warming to 2 °C. *Nature* **458**, 1158–1162 (2009).
4. Jones, C. et al. Twenty-first-century compatible CO_2 emissions and airborne fraction simulated by CMIP5 Earth system models under four representative concentration pathways. *J. Clim.* **26**, 4398–4413 (2013).
5. Collins M. et al. in *Climate Change 2013: The Physical Science Basis* (eds Stocker, T. F. et al.) Ch. 12 (Cambridge Univ. Press, Cambridge, 2013).
6. Meinshausen, M. et al. The RCP greenhouse gas concentrations and their extensions from 1765 to 2300. *Clim. Change* **109**, 213–241 (2011).
7. Millar, R. J. et al. Emission budgets and pathways consistent with limiting warming to 1.5 °C. *Nat. Geosci.* **10**, 741–747 (2017).
8. Morice, C. P., Kennedy, J. J., Rayner, N. A. & Jones, P. D. Quantifying uncertainties in global and regional temperature change using an ensemble of observational estimates: the HadCRUT4 dataset. *J. Geophys. Res.* **117**, D08101 (2012).
9. *GISS Surface Temperature Analysis (GISTEMP)* (NASA Goddard Institute for Space Studies, accessed 19 January 2017); https://data.giss.nasa.gov/gistemp/
10. Hansen, J., Ruedy, S., Sato, M. & Lo, K. Global surface temperature change. *Rev. Geophys.* **48**, RG4004 (2010).
11. Smith, T. M., Reynolds, R. W., Peterson, T. C. & Lawrimore, J. Improvements to NOAA's historical merged land–ocean surface temperature analysis (1880–2006). *J. Clim.* **21**, 2283–2296 (2008).
12. Vose, R. S. et al. NOAA's merged land–ocean surface temperature analysis. *Bull. Am. Meteorol. Soc.* **93**, 1677–1685 (2012).
13. Levitus, S. et al. World ocean heat content and thermosteric sea level change (0–2000 m), 1955–2010. *Geophys. Res. Lett.* **39**, 10 (2012).
14. Giese, B. S. & Ray, S. El Niño variability in simple ocean data assimilation (SODA), 1871–2008. *J. Geophys. Res.* **116**, C02024 (2011).
15. Balmaseda, M. A., Mogensen, K. & Weaver, A. T. Evaluation of the ECMWF ocean reanalysis system ORAS4. *Q. J. Roy. Meteorol. Soc.* **139**, 1132–1161 (2013).
16. Good, S. A., Martin, M. J. & Rayner, N. A. EN4: quality controlled ocean temperature and salinity profiles and monthly objective analyses with uncertainty estimates. *J. Geophys. Res. Ocean.* **118**, 6704–6716 (2013).
17. Smith, D. M. et al. Earth's energy imbalance since 1960 in observations and CMIP5 models. *Geophys. Res. Lett.* **42.4**, 1205–1213 (2015).
18. Cheng, L. et al. Improved estimates of ocean heat content from 1960 to 2015. *Sci. Adv.* **3**, e1601545 (2017).
19. Goodwin, P., Williams, R. G. & Ridgwell, A. Sensitivity of climate to cumulative carbon emissions due to compensation of ocean heat and carbon uptake. *Nat. Geosci.* **8**, 29–34 (2015).
20. Williams, R. G., Goodwin, P., Roussenov, V. M. & Bopp, L. A framework to understand the Transient Climate Response to Emissions. *Environ. Res. Lett.* **11**, 015003 (2016).
21. Goodwin, P. How historic simulation–observation discrepancy affects future warming projections in a very large model ensemble. *Clim. Dyn.* **47**, 2219–2233 (2016).
22. Goodwin, P., Haigh, I. D., Rohling, E. J. & Slangen, A. A new approach to projecting 21st century sea-level changes and extremes. *Earth's Future* **5**, 240–253 (2017).
23. Rohling, E. J. et al. Making sense of palaeoclimate sensitivity. *Nature* **491**, 683–691 (2012).
24. le Quéré, C. et al. Global carbon budget 2016. *Earth Syst. Sci. Data* **8**, 605–649 (2016).
25. Williamson, D. et al. History matching for exploring and reducing climate model parameter space using observations and a large perturbed physics ensemble. *Clim. Dyn.* **41**, 1703–1729 (2013).
26. Williamson, D., Blaker, A. T., Hampton, C. & Salter, J. Identifying and removing structural biases in climate models with history matching. *Clim. Dyn.* **45**, 1299 (2015).
27. Marvel, K., Schmidt, G. A., Miller, R. L. & Nazarenko, L. S. Implications for climate sensitivity from the response to individual forcings. *Nat. Clim. Change* **6**, 386–389 (2015).
28. Shindell, D. T. Inhomogeneous forcing and transient climate sensitivity. *Nat. Clim. Chang.* **4**, 274–277 (2014).

29. Hansen, J. et al. Efficacy of climate forcings. *J. Geophys. Res. Atmos.* **110**, D18104 (2005).
30. Winton, M., Takahashi, K. & Held, I. Importance of ocean heat uptake efficacy to transient climate change. *J. Clim.* **23**, 2333–2344 (2010).
31. Armour, K. C., Bitz, C. M. & Roe, G. H. Time-varying climate sensitivity from regional feedbacks. *J. Clim.* **26**, 4518–4534 (2013).
32. Gregory, J. M. & Andrews, T. Variation in climate sensitivity and feedback parameters during the historical period. *Geophys. Res. Lett.* **43**, 3911–3920 (2016).
33. Armour, K. C. Energy budget constraints on climate sensitivity in light of inconstant climate feedbacks. *Nat. Clim. Chang.* **7**, 331–335 (2017).
34. Rugenstein, M. A. A., Caldeira, K. & Knutti, R. Dependence of global radiative feedbacks on evolving patterns of surface heat fluxes. *Geophys. Res. Lett.* **43**, 9877–9885 (2016).
35. Knutti, R. & Hergerl, G. C. The equilibrium sensitivity of the Earth's temperature to radiation changes. *Nat. Geosci.* **1**, 735–743 (2008).
36. Geoffroy, O. et al. Transient climate response in a two-layer energy-balance model. Part II: Representation of the efficacy of deep-ocean heat uptake and validation for CMIP5 AOGCMs. *J. Clim.* **26**, 1859–1876 (2013).
37. Williams, R. G., Roussenov, V., Goodwin, P., Resplandy, L. & Bopp, L. Sensitivity of global warming to carbon emissions: effects of heat and carbon uptake in a suite of Earth system models. *J. Clim.* **30**, 9343–9363 (2017).
38. Allen, M. R. et al. Warming caused by cumulative carbon emissions towards the trillionth tonne. *Nature* **458**, 1163–1166 (2009).
39. Matthews, H. D., Gillet, N. P., Stott, P. A. & Zickfield, K. The proportionality of global warming to cumulative carbon emissions. *Nature* **459**, 829–832 (2009).
40. Gillet, N. P., Arora, V. K., Matthews, D. & Allen, M. R. Constraining the ratio of global warming to cumulative CO_2 emissions using CMIP5 simulations. *J. Clim.* **26**, 6844–6858 (2013).
41. Rogelj, J. et al. Paris Agreement climate proposals need a boost to keep warming well below 2 °C. *Nature* **534**, 631–639 (2016).
42. Rockström, J. et al. A roadmap for rapid decarbonisation. *Science* **355**, 1269–1271 (2017).

Acknowledgements

We acknowledge the World Climate Research Programme's Working Group on Coupled Modelling, which is responsible for CMIP, and we thank the climate modelling groups (listed in Supplementary Table 1 of this paper) for producing and making available their model output. For CMIP, the US Department of Energy's Program for Climate Model Diagnosis and Intercomparison provides coordinating support and lead development of the software infrastructure in partnership with the Global Organization for Earth System Science Portals. This work was supported by UK Natural Environment Research Council (NERC) grants NE/P01495X/1 and NE/N009789/1. G.L.F. acknowledges support from UK NERC grants NE/D00876X/2, NE/I005595/1 and NE/P011381/1. E.J.R. acknowledges Australian Laureate Fellowship FL120100050.

Author contributions

P.G. and R.G.W. led the writing of the manuscript, with contributions from all of the co-authors. P.G. conducted the numerical experiments, which were conceived by P.G. and G.L.F. E.J.R. provided the geological climate sensitivity distribution. V.M.R. analysed the CMIP5 Earth system model output. A.K. and R.G.W. analysed the ocean heat re-analysis records.

Competing interests

The authors declare no competing financial interests.

Additional information

Supplementary information is available for this paper at https://doi.org/10.1038/s41561-017-0054-8.

Correspondence and requests for materials should be addressed to P.G.

Methods

The displayed CMIP5 Earth system model output. A range of Earth system CMIP5 model results are displayed in Figs. 1, 2 and 4 and Supplementary Fig. 1, and are taken from the Earth system models in Supplementary Table 1 (refs [43–51]). Figs. 1a and 4a contain all 13 Earth system models. Figs. 1b, 2 and 4b each contain nine of the Earth system models: CanESM2, GFDL-ESM2G, GFDL-ESM2M, HadGEM2-CC, HadGEM2-ES, IPSL-CM5A-LR, MIROC-ESM, MPI-ESM-LR and NorESM1-ME. Fig. 3c contains eight of these Earth system models (it excluding HadGEM2-CC).

The efficient Earth system model. For our efficient Earth system model, we use the Warming Acidification and Sea-level Projector (WASP)[21,22]. This model is integrated 100 million times with alternative parameter combinations to find simulations that agree with historic observational constraints (Supplementary Table 2). As configured in Goodwin[21] and Goodwin et al.[22], WASP lacks stochastic behaviour in the global surface temperature anomaly. However, the observational constraints for surface warming (Supplementary Table 3) represent both the underlying trends and internal stochastic variability in the climate system. Therefore, model simulations that accurately represent the underlying trends in historic surface warming but lack stochastic behaviour still may not be consistent with the observational constraints. To maximize the possibility of including model simulations that both accurately represent the underlying trends in surface warming and agree with observations, we employ an additional stochastic surface temperature anomaly in WASP, applied to global mean surface air temperature (T) and global mean sea surface temperature (SST).

As global temperature anomaly records are generally presented with a one-month resolution[8–12], we employed a monthly time-step in WASP (altered from the ten per year[21,22]). A stochastic temperature anomaly, $T_{\text{stochastic}}$ (°C), was then inserted into surface air temperatures and SSTs using a noise distribution (AR(2) noise),

$$T_{\text{stochastic}}(t) = c_1 T_{\text{stochastic}}(t-dt) + c_2 T_{\text{stochastic}}(t-2dt) + c_3 z_i(t) \quad (2)$$

where δt is the one-month model time step, c_1, c_2 and c_3 are non-dimensional tuned constants and z_i is a randomly assigned temperature anomaly between −1.0 and 1.0 K. The coefficients c_1, c_2 and c_3 are tuned such that the simulated monthly global surface temperature anomaly has similar amplitude and autocorrelation properties to the monthly GISTEMP record between years 1971 and 2016. This is assessed by removing the linear trend in the NASA GISTEMP[9] monthly record from year 1971 to year 2016 to reveal the autocorrelation properties and the amplitude, with the variability having a root mean square of 0.14 °C. For comparison, the first 20 simulations accepted into the standard experiment observation-consistent ensemble using RCP8.5 considered from year 1971 to year 2016. With the linear trends in warming removed, the 20 simulations have an average root mean square amplitude variability of 0.13 °C, with a standard deviation of 0.04 °C between simulations, when using coefficient values tuned to $c_1 = 0.3$, $c_2 = 0.4$ and $c_3 = 0.062$. These root mean square amplitude variability values of the 20 simulations are similar to the 0.14 °C value for the GISTEMP observations, and the simulations display similar autocorrelation properties.

Generating the observation-consistent model ensembles. A total of ten model ensembles are constructed, each of which contains ~3×10^4 observation-consistent simulations. These ten model ensembles comprise four ensembles using a standard experimental set-up for each of four forcing scenarios, RCP8.5, RCP6.0, RCP4.5 and RCP2.6, and a further six ensembles using alternative experimental set-ups that all follow the RCP8.5 scenario.

First, an initial prior ensemble[21] of 10^8 model configurations is constructed by independently varying 18 model parameters with specified prior distributions (Supplementary Table 2 for experiment 1, and Supplementary Table 3 shows how this configuration is changed for the other experiments). These model 18 varied model parameters that represent the physical, chemical and biological properties of our efficient Earth system model. Each model configuration is then forced with historic CO_2 and radiative forcing followed by RCP scenarios from Meinshausen et al.[6]. In each of the initial 10^8 simulations, the three radiative forcing terms, from CO_2, other Kyoto agents (comprising well-mixed greenhouse gases other than CO_2 and chlorofluorocarbons) and non-Kyoto agents (principally aerosols)[6], are independently varied with normal distributions, such that the distributions in year 2011 approximate the uncertainty in the three radiative forcing terms as assessed by the IPCC[2] (Supplementary Table 2). The radiative forcing from well-mixed greenhouse gases other than CO_2 and aerosols (and non-Kyoto agents) are both varied using scaling coefficients that apply over all time to each property respectively (Supplementary Fig. 2). The input distribution for the initial 10^8 simulations for the climate sensitivity, S, is drawn from a probability distribution for the value of S in palaeoclimates assessed from a review of geological evidence over the Cenozoic[23], using the distribution with log-normal uncertainty (Fig. 3, black solid lines).

At the end of year 2016, each of the 10^8 simulations are assessed using an observational-consistency test[21,22] that covers nine observational constraints for surface warming[8–12,52,53], ocean heat uptake[13–18,54–57] and carbon cycle fluxes[2,58–60] (Supplementary Table 4). A simulation passes the observation-consistency test if either all nine simulated properties lie within the observed ranges (Supplementary Table 3), or if the total fractional sum of discrepancies from the observational ranges, δ_{error}, is less than 0.1. The fractional sum of discrepancies term, δ_{error}, is calculated from a summation over all observational constraints for which the simulated value lies outside the observational range (Supplementary Table 4) using:

$$\delta_{\text{error}} = \sum \left(\frac{|x_i - y_i|}{\Delta_{yi}} - 1 \right) \quad (3)$$

where x_i is the simulated model value, y_i is the midpoint of the observational constraint range, Δ_{yi} is the observation-consistent range in the observational constraint (that is, from the minimum to maximum value in Supplementary Table 4) and δ_{error} is summed only over those i constraints for which x_i lies outside the observational consistent region, $y_i \pm 0.5\Delta_{yi}$. This inclusion of simulations in the final posterior distribution provided $\delta_{\text{error}} < 0.1$ (equation (3)) allows some tolerance for simulations to be considered observationally consistent, and so removes potential bias that might arise from applying artificially narrow observational constraints when selecting the final model ensemble.

In the standard experiment, the prior input distribution for the efficacy of heat uptake ε_N is normal, with the mean and standard deviation from the distribution of 16 CMIP5 models analysed by Geoffroy et al.[36] (Supplementary Fig. 3 and Supplementary Table 2), whereas the prior input distribution for the efficacy of aerosol radiative forcing $\varepsilon_{\text{aero}}$ is uniform, ranging from 0.33 to 3.0 (Supplementary Fig. 4 and Supplementary Table 2). However, the posterior distribution of $\varepsilon_{\text{aero}}$ sees values concentrated towards one, whereas the posterior distribution of ε_N stays close to the prior input distribution from CMIP5 models (Supplementary Fig. 3).

Perturbation experiments are conducted with different input parameter distributions (Supplementary Table 5). For all the experiments except experiment 7, only 0.03% of the initial ensemble simulations pass the observation-consistency test, to produce a final observation-consistent ensemble of 3×10^4 simulations. This observation-consistent ensemble displays good agreement with the full ranges for all the observational quantities (Supplementary Table 4), which demonstrates that the 3×10^4 simulations have a good coverage of observational parameter space. For experiment 7, 0.08% of the initial ensemble passes the observation-consistency test, and thus requires only 4×10^7 initial simulations to produce ~3×10^4 observation-consistent simulations. This reduction in the number of simulations required is because any given simulation is more likely to be observationally consistent when $\varepsilon_{\text{aero}} = 1$ (Supplementary Fig. 3, which shows peak value in the posterior distribution of $\varepsilon_{\text{aero}}$ in the standard experiment).

Generating the observational-consistency test. The observational constraint ranges follow the 90–95% confidence interval for each property and where a single constraint is based on multiple records, the allowable range is widened to encompass the confidence ranges of each observational record. The nine observational constraints in the observational -consistency test are listed in Supplementary Table 3. The ocean heat uptake constraints are based on the observational records in Supplementary Table 4. To generate the limits of the ocean heat uptake constraints, we consider the range from the minimum to maximum of the individual observation reconstructions, including the 2σ uncertainty (Fig. 1c,d).

The surface air temperature constraint from years 1850–1900 to 2003–2012 is the estimated 90% confidence range from AR5 (ref. [2]). The surface air temperature constraints from years 1951–1960 to 2007–2016 and 1971–1980 to 2007–2016 are based on the HadCRUT4, GIST

EMP and NCDC records[8–12]. The 2σ error in the decadal temperatures from the HadCRUT4 record is estimated at ±0.05 °C from 1950 to the present[8], whereas the 2σ error in the annual GISTEMP record is also estimated at ±0.05 °C (ref. [10]). Therefore, we estimate a 95% confidence range in the surface air temperature constraints from 1951–1960 to 2007–2016 and from 1971–1980 to 2007–2016 by allowing an additional ±0.05 °C relative to the minimum and maximum of the HadCRUT4, GISTEMP and NCDC records, noting that the HadCRUT4 and GISTEMP records represent the minimum and maximum values for both constraints, respectively.

The SST constraint from years 1850–1900 to 2003–2012 is based on the average of the HadSST3 (accessed from https://crudata.uea.ac.uk/cru/data/temperature/ on 19 January 2017)[53] and NCDC ERSST (accessed from https://www.ncdc.noaa.gov/monitoring-references/faq/anomalies.php on 19 January 2017)[53] records, but with ±0.06 K uncertainty to mimic the 90% confidence uncertainty in global surface air temperatures over the same period from AR5. The ocean and terrestrial carbon-uptake constraints derive from AR5 assessments[2].

Calculation of global surface temperature anomalies. The Earth system model temperature anomalies are calculated relative to the 1861–1900 period. The observational temperature anomalies are calculated relative 1850–1900 for the HadCRUT4 record, and relative to 1880–1900 for the NCDC and GISTEMP records (which begin in 1880). For the efficient Earth system model, the surface temperature anomaly is calculated relative to the simulated 1850–1900 time average separately in each simulation, except for Supplementary Fig. 4 and

Supplementary Table 8 in which the temperature anomaly is calculated relative the pre-industrial steady state of the model before radiative forcing is imposed.

Code availability. The computer code for our efficient Earth system model, the Warming Acidification and Sea-level Projector, is available within the supplementary material for this manuscript.

Data availability. Data that supports this study has been deposited in the British Oceanographic Data Centre published data library database (dataset title: "Observation consistent warming projections for 2081–2100 from the WASP model for the RCP4.5 scenario, and the corresponding earth system properties"). All other data that support this study are available within the supplementary material of this manuscript.

References

43. Arora, V. K. et al. Carbon emission limits required to satisfy future representative concentration pathways of greenhouse gases. *Geophys. Res. Lett.* **38**, L046270 (2011).
44. Moore, J., Lindsay, K., Doney, S., Long, M. & Misumi, K. Marine ecosystem dynamics and biogeochemical cycling in the Community Earth System Model [CESM1(BGC)]: comparison of the 1990s with the 2090s under the RCP4.5 and RCP8.5 scenarios. *J. Clim.* **26**, 9291–9312 (2013).
45. Dunne, J. P. et al. GFDLs ESM2 global coupled climate carbon Earth system models. Part II: Carbon system formulation and baseline simulation characteristics. *J. Clim.* **26**, 2247–2267 (2013).
46. Martin, G. M. et al. The HadGEM2 family of Met Office Unified Model climate configurations. *Geosci. Model. Dev.* **4**, 723–757 (2011).
47. Jones, C. D. et al. The HadGEM2-ES implementation of CMIP5 centennial simulations. *Geosci. Model. Dev.* **4**, 543–570 (2011).
48. Dufresne, J. L. et al. Climate change projections using the IPSL-CM5 Earth system model: from CMIP3 to CMIP5. *Clim. Dyn.* **40**, 2123–2165 (2013).
49. Watanabe, S. et al. MIROC-ESM 2010: model description and basic results of CMIP5-20c3m experiments. *Geosci. Model. Dev.* **4**, 845–872 (2011).
50. Giorgetta, M. A. et al. Climate and carbon cycle changes from 1850 to 2100 in MPI-ESM simulations for the Coupled Model Intercomparison Project phase 5: climate changes in MPI-ESM. *J. Adv. Model. Earth Syst.* **5**, 572–597 (2013).
51. Tjiputra, J. F. et al. Evaluation of the carbon cycle components in the Norwegian Earth System Model (NorESM). *Geosci. Model. Dev.* **6**, 301–325 (2013).
52. Kennedy, J. J., Rayner, N. A., Smith, R. O., Saunby, M. & Parker, D. E. Reassessing biases and other uncertainties in sea-surface temperature observations measured in situ since 1850. Part 2: Biases and homogenisation. *J. Geophys. Res.* **116**, D14104 (2011).
53. Huang, B. et al. Extended Reconstructed Sea Surface Temperature Version 4 (ERSST.v4). Part I: Upgrades and intercomparisons. *J. Clim.* **28**, 911–930 (2015).
54. Domingues, C. M. et al. Improved estimates of upper-ocean warming and multi-decadal sea-level rise. *Nature* **453**, 1090–1093 (2008).
55. Ishii, M. & Kimoto, M. Reevaluation of historical ocean heat content variations with an XBT depth bias correction. *J. Oceanogr.* **65**, 287–299 (2009).
56. Smith, D. M. & Murphy, J. M. An objective ocean temperature and salinity analysis using covariances from a global climate model. *J. Geophys. Res.* **112**, C02022 (2007).
57. Carton, J. A. & Giese, B. S. A reanalysis of ocean climate using Simple Ocean Data Assimilation (SODA). *Mon. Weather. Rev.* **136**, 2999–3017 (2008).
58. Boden, T. A., G. Marland, and R. J. Andres. *Global, Regional, and National Fossil-Fuel CO_2 Emissions* (Carbon Dioxide Information Analysis Center, Oak Ridge National Laboratory, TN, 2016); https://doi.org/10.3334/CDIAC/00001_V2016.
59. Houghton, R. A. et al. Chapter G2 carbon emissions from land use and land-cover change. *Biogeosciences* **9**, 5125–514 (2012).
60. Khatiwala, S. et al. Global ocean storage of anthropogenic carbon. *Biogeosciences* **10**, 2169–2191 (2013).